



## Numerical simulations of CO<sub>2</sub> absorption by MgO-based sorbent in a gas–solid fluidized bed

Linhang Zhu<sup>a</sup>, Chang Liu<sup>a</sup>, Chenghang Zheng<sup>a,b,d</sup>, Shihan Zhang<sup>c</sup>, Haidong Fan<sup>b</sup>, Kun Luo<sup>a</sup>, Xiang Gao<sup>a,b,c,d,\*</sup>

<sup>a</sup> State Key Lab of Clean Energy Utilization, Institute of Carbon Neutrality, State Environmental Protection Engineering Center for Coal-Fired Air Pollution Control, Zhejiang University, Hangzhou 310027, China

<sup>b</sup> Zhejiang Baima Lake Laboratory Co., Ltd., Hangzhou 310051, China

<sup>c</sup> Zhejiang University of Technology, Hangzhou 310014, China

<sup>d</sup> Jiaying Research Institute, Zhejiang University, Jiaying 314000, China

### ARTICLE INFO

Editor: S Yi

#### Keywords:

CO<sub>2</sub> capture  
Two-way coupled CFD-DEM simulation  
Solid sorbent absorption  
Decarbonization performance

### ABSTRACT

Given that carbon dioxide (CO<sub>2</sub>) constitutes the predominant proportion of greenhouse gas emissions, its capture, utilization and storage have always been a subject of great concern. Gas-solid fluidized bed has become one of the commonly applied equipment for the removal of CO<sub>2</sub> from flue gases owing to its advantages such as exceptional mixing effect and substantial interfacial area between the phases. However, there is a lack of attention to the mechanism of CO<sub>2</sub> absorption by individually-tracked moving solid sorbents as well as their effects on the decarbonization performance in a gas–solid fluidized bed. In this study, CO<sub>2</sub> removal model by solid particles based on MgO adsorbent was established with the implementation of the shrinking-core model and each particle was tracked individually. Results validated the accuracy of the absorption model and revealed that smaller sizes of the solid adsorbent, lower inlet gas velocities and larger inlet CO<sub>2</sub> mass fractions exhibit relatively high CO<sub>2</sub> removal efficiency. In addition, the decarbonization performance of fluidized and packed beds was compared. The packed bed exhibits more uniform gas flow and higher CO<sub>2</sub> removal efficiency, whereas the fluidized bed provides larger interphase contact area, which facilitates the heat transfer process. Through the analysis of a series of parameters, the results provide recommendations for improving the CO<sub>2</sub> removal efficiency and help to explore the optimal protocol for the design of bed reactors for CO<sub>2</sub> removal.

### 1. Introduction

Over the past few decades, the excessive emissions of greenhouse gases have resulted in severe global warming and climate change. Given that carbon dioxide (CO<sub>2</sub>) constitutes the predominant proportion of greenhouse gas emissions, many countries and regions have enacted a series of emission limits: more than 110 other countries have pledged to achieve carbon neutrality by 2050; China has also committed to reaching this goal of carbon neutrality by 2060. Despite the prediction that fossil fuels will remain the worldwide-dominant source of energy at least the next decade [1,2], imperative strategies on CO<sub>2</sub> mitigation have emerged, one of which is the widespread deployment of valorization technologies for captured CO<sub>2</sub> [1]. Towards Carbon-neutral and Net-zero emissions in a sustainable way, CO<sub>2</sub> capture and valorization technologies have become highly concerned topics [3,4].

Common CO<sub>2</sub> capture techniques include gas–liquid adsorption, gas–solid adsorption, cryogenic distillation [5] and membrane separation [6]. The gas–liquid absorption method is one of the most mature and promising technologies for industrialization since it provides high CO<sub>2</sub> removal rate [7]. However, this method suffers from inherent defects such as equipment corrosion and high energy consumption in the desorbing section [8]. Despite its relatively low CO<sub>2</sub> removal rate, the gas–solid method as an alternative method has been widely applied due to its advantage of requiring lower energy and operation temperature [9–11]. Consequently, as a crucial criterion for assessing the decarbonization performance, improving the CO<sub>2</sub> removal efficiency of gas–solid fluidized is of great importance and has attracted the attention of many researchers. To figure out the impacting factors on CO<sub>2</sub> removal efficiency and to access enhanced methods, a sequence of experiments has been conducted.

In recent research, the most commonly applied sorbents are

\* Corresponding author.

E-mail address: [xgao1@zju.edu.cn](mailto:xgao1@zju.edu.cn) (X. Gao).

<https://doi.org/10.1016/j.seppur.2024.127381>

Received 1 February 2024; Received in revised form 26 March 2024; Accepted 3 April 2024

Available online 4 April 2024

1383-5866/© 2024 Elsevier B.V. All rights reserved.

**Nomenclature**

$C_b(\text{mol}/\text{m}^3)$	CO <sub>2</sub> concentration in the bulk gas
$C_D(-)$	Drag coefficient for an isolated particle
$C_e(\text{mol}/\text{m}^3)$	Equilibrium CO <sub>2</sub> concentration
$D_g(\text{m}^2/\text{s})$	Diffusion coefficient of gas
$D_{g0}(\text{m}^2/\text{s})$	initial diffusion coefficient
$d_p(\text{m})$	Particle diameter
$f_c(\text{N})$	Contact force
$f_d(\text{N})$	Drag force
$f_{p,g}(\text{N})$	Interaction force between phases
$g(\text{m}/\text{s}^2)$	Gravity acceleration
$H_g(\text{J}/\text{kg})$	Gas enthalpy
$I_{gm}(\text{N}/\text{m}^3)$	Coupling term between phases
$I_p(\text{kgm}^2)$	Particle inertia
$J_i(\text{kg}/(\text{m}^2\cdot\text{s}))$	Diffusion flux of species i
$k_s(\text{m}/\text{s})$	Reaction constant
$m_p(\text{kg})$	Particle mass
$N_{\text{MgO}}^0(\text{N}/\text{m}^3)$	Initial number of moles of MgO per unit volume
$N_i(\text{kg}/(\text{m}\cdot\text{s}))$	Production net rate
$Re(-)$	Reynolds number
$r_{\text{CO}_2}(\text{mol}/(\text{m}^2\cdot\text{s}))$	Reaction rate of CO <sub>2</sub>
$r_c(\text{m})$	Low-reactive zone radius
$r_i(\text{m})$	Unreacted solid sorbent particle radius

$r_p(\text{m})$	Initial particle radius
$r'_p(\text{m})$	Expanded radius of the sorbent particle
$S_h(-)$	Energy source
$S_{Y_i}(\text{kg}/(\text{m}\cdot\text{s}))$	Rate of creation by addition plus any user-defined sources
$T_r(\text{Nm})$	Rolling friction torque
$u_g(\text{m}/\text{s})$	Gas velocity
$u_p(\text{m}/\text{s})$	Particle velocity
$V_p(\text{m}^3)$	Particle volume
$X(-)$	Conversion rate
$Y_i(-)$	Mass fraction of species i
$Z(-)$	Expansion factor

**Greek letters**

$\alpha(-)$	Adjustable parameter for diffusion coefficient
$\beta(-)$	Fluid-particle drag coefficient
$\beta_g(-)$	Adjustable parameter for diffusion coefficient
$\delta_i(\text{m})$	Thickness of high-reactive zone
$\varepsilon_g(-)$	Gas volume fraction
$\mu_g(\text{Pa}\cdot\text{s})$	Viscosity of the gas phase
$\rho_g(\text{kg}/\text{m}^3)$	Density of the gas phase
$\tau_g(\text{N}/\text{m}^2)$	Stress tensor of the gas phase
$\omega_p(\text{rad}/\text{s})$	Angular velocity of solid particles

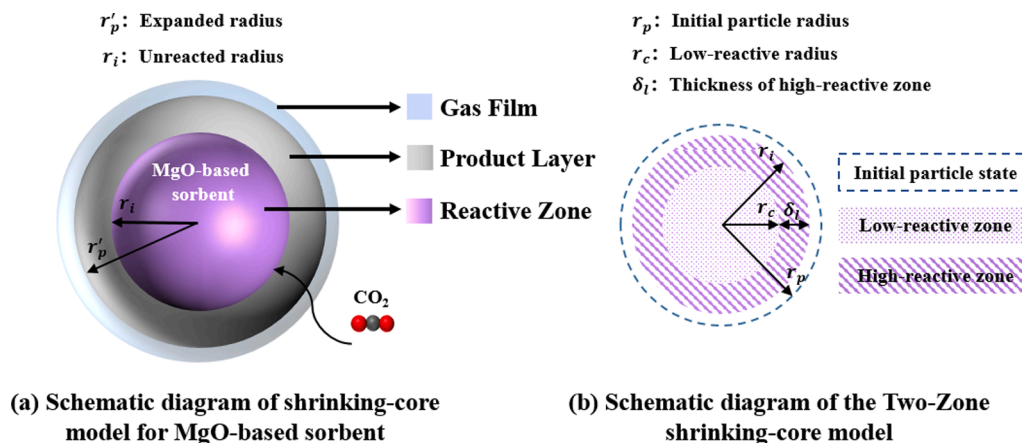


Fig. 1. Schematic diagrams of the reaction model for MgO-based sorbent.

magnesium-based [12–17] and potassium-based [8,11,18] sorbents. To design the carbonization absorber, different parameters (including temperature, carbonator space time, Ca looping ratio) were investigated in quartz fixed bed [19] and DFB facility [20]. For the design of CO<sub>2</sub> removal in a circulating fluidized bed (CFB), Benjapon et al. [21] experimentally determined the sorption rates of CO<sub>2</sub> based on potassium carbonate sorbent using a kinetic theory based hydrodynamic model. Ayoobi et al. [22] employed a laboratory-scale bubbling gas–solid fluidized bed to gain deeper insights into the fluid dynamics and adsorption kinetics using K<sub>2</sub>CO<sub>3</sub> based sorbent particles by experiments as well as numerical simulations. Hassanzadeh et al. [12–14] extended the variable diffusivity model by incorporating the physically expanding product layer and two reacting zones to describe the gas–solid decarbonation reaction.

However, practical problems were faced in experimental studies. For example, to understand the gas–solid flow behaviors and determine the optimum parameters of the fluidized bed such as sorbent particle

diameter, inner structure, etc., the analyses of flow characteristics and transient particle behaviors are necessary, which are difficult to be obtained by experimental results. The computation methods provide powerful and attractive complementary approach to laborious experimental studies in an economically feasible way [23]. Generally, the simulation model of gas–solid absorption could be divided into two classifications: Eulerian-Eulerian and Eulerian-Lagrangian model. Based on Eulerian-Eulerian model, both solid phase and gas phase are regarded as the continuous phase. By using Eulerian-Eulerian model, researchers mainly focused on the adsorber performance with respect to heat removal efficiency, gas flow rate, solids circulation rate [24], and reaction kinetics [18], etc. Abbasi et al. [15] proposed a novel two-way coupled CFD-PBE model along with the two-zone variable diffusivity shrinking core reaction model for CO<sub>2</sub> capture in a circulating fluidized bed. As for Eulerian-Lagrangian model, the gas phase is regarded as the dispersed phase, of which the motion is calculated individually to obtain the moving trajectory and distribution in the fluidized bed reactor.

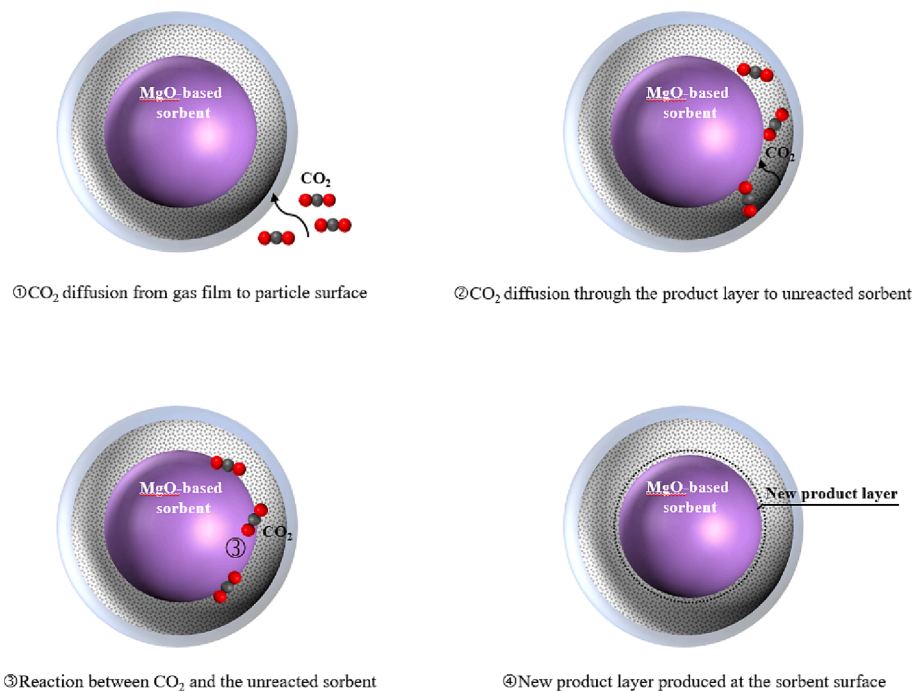


Fig. 2. Reaction mechanism of CO<sub>2</sub> absorption by MgO-based sorbent.

Table 1  
Simulation parameters of the bed.

Parameters	Values
Mesh grid size (mm)	2.7 d <sub>p</sub>
Bed size (Length*width*height)(mm)	(22*2.7 d <sub>p</sub> )*(3.7*2.7 d <sub>p</sub> ) * (100*2.7d <sub>p</sub>
Gas density	Ideal gas
Viscosity/ Thermal conductivity/ Specific heat capacity	Mass-weighted mixing law
Temperature (K)	673
Inlet CO <sub>2</sub> mass fraction	0.5
Particle diameter (mm)	0.5, 1, 2, 3
Particle density (kg/m <sup>3</sup> )	2545

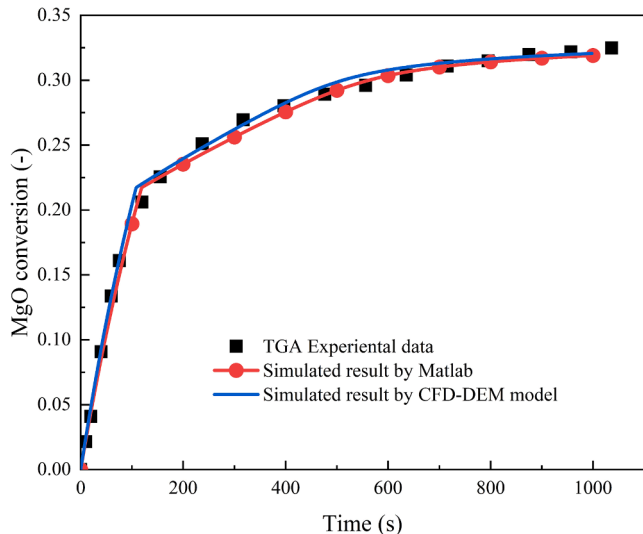


Fig. 3. Comparison of TGA experimental results against the simulated sorbent conversion rate (d<sub>p</sub> = 255 μm, T = 698 K).

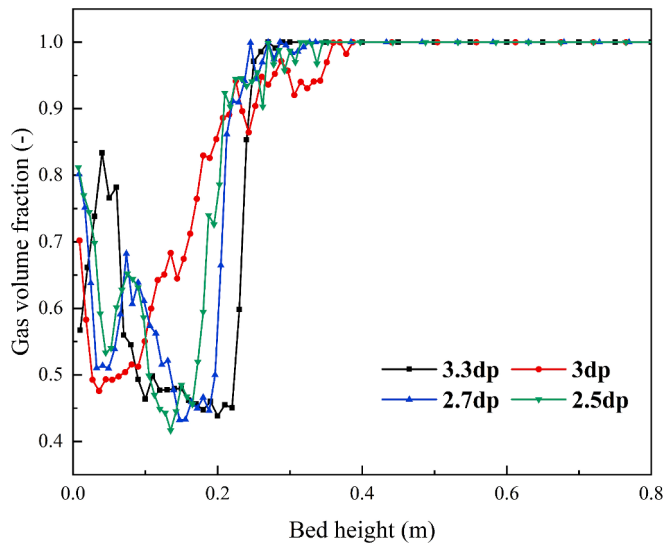


Fig. 4. Mesh dependence test.

Commercially available Barracuda® software package [25,26] and FLUENT® software were most commonly applied to study the hydrodynamics and CO<sub>2</sub> adsorption in the certain reactor. To achieve the bubble-free fluidization, a plug flow model has been proved as a reliable first approximation for achieving bubble-free using two binary mixtures of 75 and 375 μm particles [27].

To summarize, previous studies have primarily concentrated on the overall CO<sub>2</sub> removal performance and flow field behavior, with less attention paid to the detailed motion of particles. Most studies apply the two-fluid model (TFM), ignoring the moving trajectories and decarbonization performance of solid particles. This leaves a significant gap in understanding the specific movements and decarbonization effects of solid sorbents. In addition, the implementation of CO<sub>2</sub> adsorption model by solid sorbent particles is limited in the current simulations of gas–solid fluidized beds that apply commercial software packages.

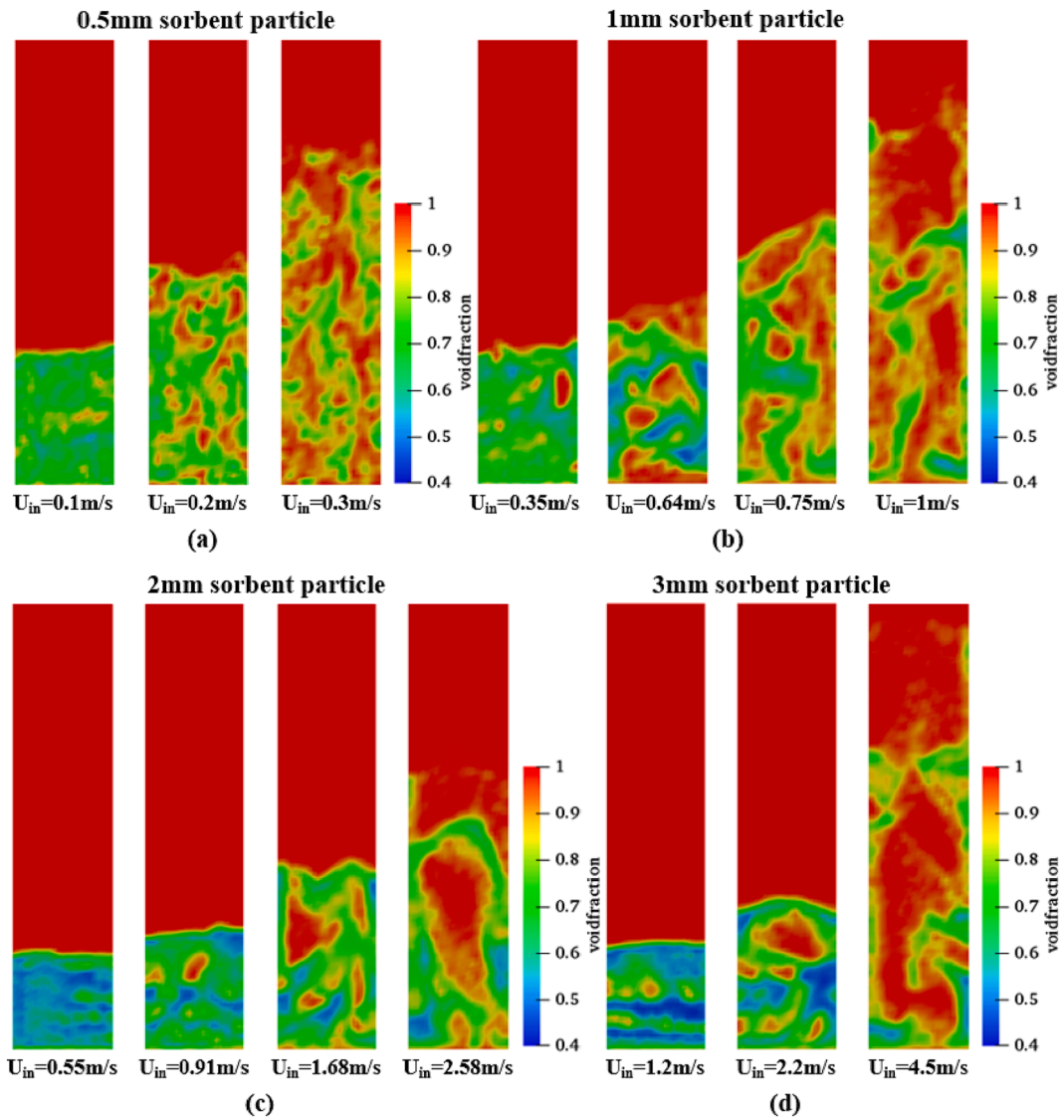


Fig. 5. Instantaneous contour of gas volume fraction for varying sorbent particle sizes and inlet velocities.

Unlike the commonly applied TFM model, our research utilizes two-way coupled CFD-DEM numerical simulations with open-source software to track each particle individually within a gas–solid fluidized bed. The CO<sub>2</sub> removal model based on MgO sorbents was established with the implementation of shrinking-core model and the moving trajectory of each particle was recorded. Since pioneering researchers have already focused on some of the impacting factors on the decarbonization performance and removal efficiency in the fluidized bed, for instance, particle radius, inlet gas velocity, inlet CO<sub>2</sub> concentration, gas temperature, etc., similar parameters were conducted to verify the accuracy of the self-developed CO<sub>2</sub> removal solver based on CFD-DEM model. The goal is to access the impact of different parameters, thereby offering recommendations for improving the CO<sub>2</sub> removal efficiency and the design of bed reactors for the removal of CO<sub>2</sub> by solid sorbent particles.

## 2. Numerical models

For the numerical simulations conducted in this study, two-way coupled CFD-DEM MPI method was utilized. The gas phase was treated as the continuous phase while the solid phase was treated as the dispersed phase. MgO-based sorbent was chosen to absorb CO<sub>2</sub> from the gas phase and the shrinking core model is implemented to describe the absorption process. Further details can be found in the governing

equations specified in the following sub-sections:

### 2.1. Gas phase

The continuum equation, Navier-Stokes equation (momentum balance equation), and energy balance equation were employed to solve the gas phase [28,29]:

$$\frac{\partial}{\partial t}(\varepsilon_g \rho_g) + \nabla \cdot (\varepsilon_g \rho_g \mathbf{u}_g) = 0 \quad (1)$$

$$\frac{\partial}{\partial t}(\varepsilon_g \rho_g \mathbf{u}_g) + \nabla \cdot (\varepsilon_g \rho_g \mathbf{u}_g \mathbf{u}_g) = -\varepsilon_g \nabla p + \nabla \cdot \boldsymbol{\tau}_g + \varepsilon_g \rho_g \mathbf{g} - \sum_{m=1}^M \mathbf{J}_{gm} \quad (2)$$

$$\frac{\partial}{\partial t}(\varepsilon_g \rho_g H_g) + \nabla \cdot (\varepsilon_g \rho_g H_g \mathbf{u}_g) = \nabla \cdot (\varepsilon_g k \nabla T) + h_{gp}(T_g - T_p) + S_h \quad (3)$$

where  $\varepsilon_g$ ,  $\rho_g$ ,  $\mathbf{u}_g$  stand the volume fraction, density and velocity of the gas phase, respectively;  $p$  is the pressure,  $\boldsymbol{\tau}_g$  represents the stress tensor of the gas phase,  $\mathbf{J}_{gm}$  stands the coupling term between the two phases;  $H_g$  and  $k$  are the enthalpy and thermal conductivity of the gas phase, respectively;  $h_{gp}$  represents the interphase heat transfer coefficient, and  $S_h$  is the energy source term. For the gas phase,  $S_h$  represents the heat released by

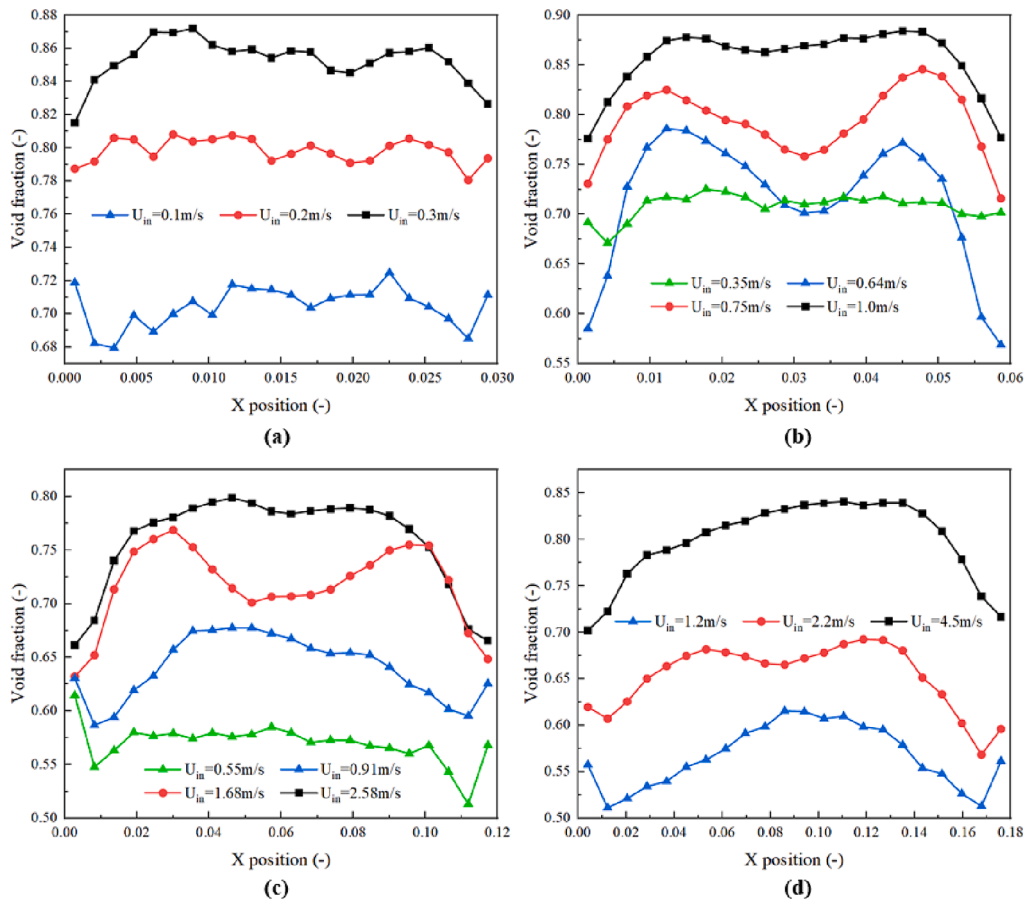


Fig. 6. Time-averaged void fraction for different sizes of sorbents and varying inlet gas velocities.

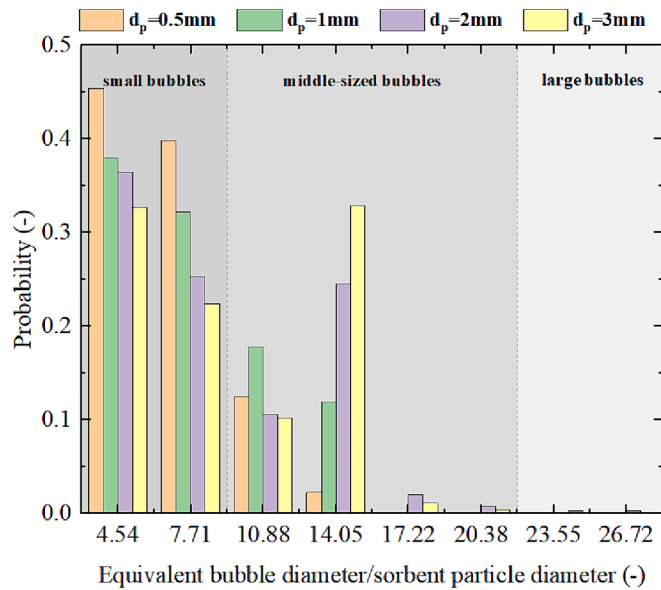


Fig. 7. Equivalent bubble diameter/sorbent particle diameter for varying sizes of sorbent particles.

the chemical reaction. Since the chemical reaction heat is omitted,  $S_h$  is assumed to be 0 in this equation.

The species transport equation is listed as the following:

$$\frac{\partial}{\partial t}(\epsilon_g \rho_g Y_i) + \nabla \cdot (\epsilon_g \rho_g Y_i \mathbf{u}_g) = \nabla \cdot \mathbf{J}_i + N_i + S_{Y,i} \quad (4)$$

where  $Y_i$ ,  $J_i$  are the mass fraction and diffusion flux of the  $i$ th species, respectively.  $N_i$  represents the net rate of the species  $i$  that is produced by the reaction,  $S_{Y,i}$  is the rate produced by the solid particles.

## 2.2. Solid phase

For the dispersed phase, the moving trajectory of each individual solid sorbent particle is determined by applying Newton's Second Law, with its translational equation as well as the angular momentum equation provided as follows [23]:

$$m_p \frac{d\mathbf{u}_p}{dt} = \mathbf{f}_c^n + \mathbf{f}_c^t + \mathbf{f}_{p,g} + m_p \mathbf{g} \quad (5)$$

$$I_p \frac{d\boldsymbol{\omega}_p}{dt} = \mathbf{T}_r + \mathbf{T}_t \quad (6)$$

Where  $m_p$  represents the particle mass;  $T_r$  and  $T_t$  respectively denote the rolling friction torque and tangential torque;  $I_p$  is the moment of inertia of the sorbent particles;  $f_c^n$  and  $f_c^t$  correspondingly refer to the normal contact force and tangential contact force;  $\mathbf{u}_p$  and  $\boldsymbol{\omega}_p$  indicate the translational velocity and angular velocity of the sorbent particles;  $\mathbf{f}_{p,g}$  is the total interaction force exerted by the continuous phase.

In this study, the hertz contact model is applied to describe the collision between particles. The contact forces between particles were based on Hertz contact model, as shown below [30,31]:

$$\mathbf{f}_n = -k_n \delta_n \mathbf{n}_c - \gamma_n \cdot (\mathbf{v}_c \cdot \mathbf{n}_c) \mathbf{n}_c \quad (7)$$

$$\mathbf{f}_t = \min[-k_t \delta_t \mathbf{t}_c - \gamma_t \cdot (\mathbf{v}_c \cdot \mathbf{n}_c) \mathbf{t}_c, f_s \mathbf{f}_n \mathbf{t}_c] \quad (8)$$

where  $\mathbf{f}_n$  denotes the normal force and  $\mathbf{f}_t$  denotes the tangential force;  $k_n$ ,

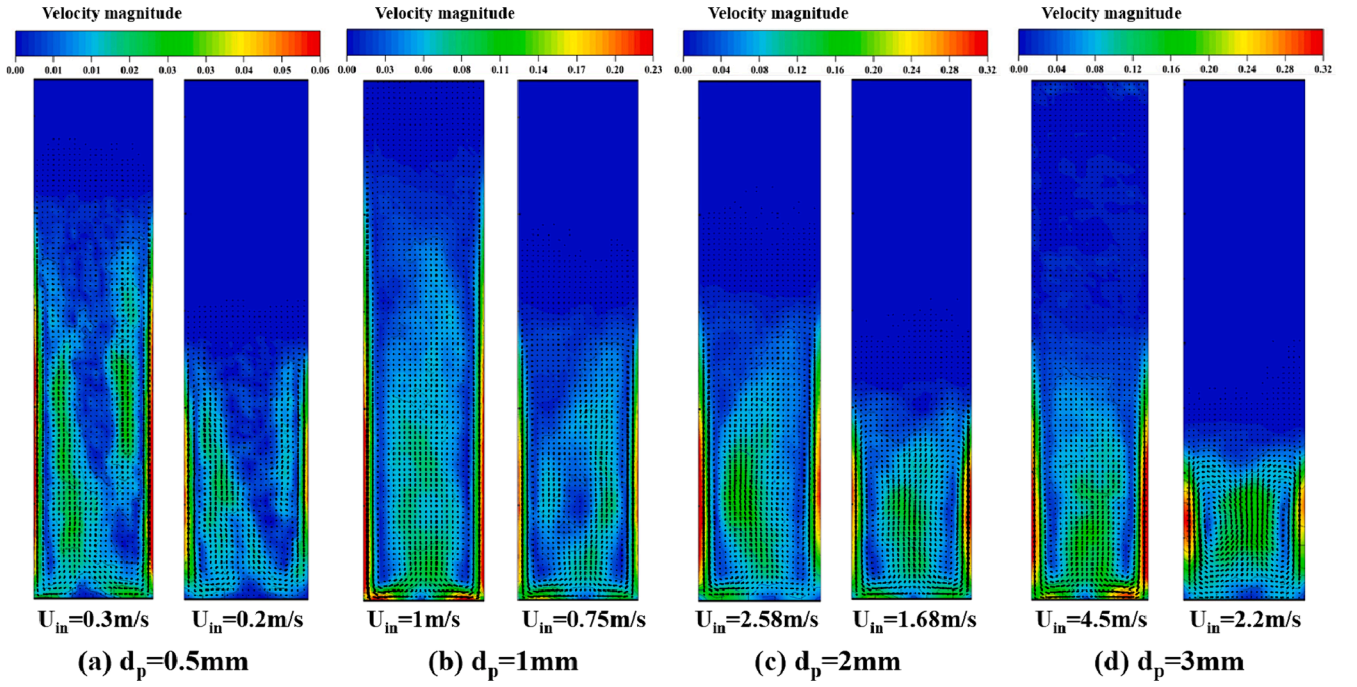


Fig. 8. Time-averaged particle velocity vector and contour for different sizes of sorbent particles.

$k_t$ ,  $\gamma_n$  and  $\gamma_t$  represent the normal and tangential stiffness coefficients and viscoelastic damping coefficients respectively;  $\delta_n$  and  $\delta_t$  represent the normal and tangential overlap distances of two particles;  $f_s$  is the sliding friction coefficient.

### 2.3. Phase interaction

In this study, it is hypothesized that the dominant interaction force between sorbent particles and gas phase is drag force. Gidaspow model is preferred [32] in this study, and the expressions could be written as the following [33]:

$$f_d = \frac{V_p \beta (\mathbf{u}_g - \mathbf{u}_p)}{(1 - \varepsilon_g)} \quad (9)$$

where  $V_p$  is the sorbent particle volume,  $\beta$  stands for the fluid-particle drag coefficient:

$$\beta = \begin{cases} 150 \frac{(1 - \varepsilon_g)^2 \mu_g}{\varepsilon_g d_p^2} + 1.75 \frac{\rho_g (1 - \varepsilon_g) |\mathbf{u}_g - \mathbf{u}_p|}{d_p} & \varepsilon_g < 0.8 \\ \frac{3}{4} C_D \frac{\rho_g (1 - \varepsilon_g) |\mathbf{u}_g - \mathbf{u}_p|}{d_p} \varepsilon_g^{-2.65} & \varepsilon_g \geq 0.8 \end{cases} \quad (10)$$

where  $d_p$  represents the diameter of the sorbent particle; the drag coefficient of the particle, denoted as  $C_D$ , is determined by the Schiller & Naumann correlation:

$$C_D = \begin{cases} \frac{24}{Re} (1 + 0.15 Re^{0.687}) & Re < 1000 \\ 0.44 & Re \geq 1000 \end{cases} \quad (11)$$

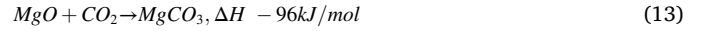
where the  $Re$  stands for Reynolds number and is defined as:

$$Re = \frac{\rho_g \varepsilon_g d_p |\mathbf{u}_g - \mathbf{u}_p|}{\mu_g} \quad (12)$$

### 2.4. Decarbonization model

In this study, the decarbonization process is based on the absorption

process of MgO-based sorbent and the chemical reaction equation could be summarized as follows [12]:



For the process of  $CO_2$  absorption by the solid sorbent particle, the shrinking-core model is applied. The solid sorbent particle is assumed to be spherical, as illustrated in Fig. 1(a), the absorption process occurs on the surface of the particle, with the generated product layer depositing on the outer layer of the particle. The sorbent particle consists of three parts: the gas film, the product layer and the reactive zone. Fig. 1(b) illustrates the schematic diagram of the reactive zone: the core of the sorbent particle is the low reactive zone, which is wrapped by the highly reactive zone with a thickness of  $\delta_l$ . When the reaction occurs on the surface of the highly reactive zone, the reaction rate is relatively high; once the highly reactive zone is consumed, the reaction occurs on the surface of the low reactive zone with a relatively low reaction rate.

The overall reaction process could be divided into several main steps as depicted in Fig. 2 [11,13]:

- Gaseous reactant ( $CO_2$ ) diffuses from the gas film to reach the solid sorbent particles' surface;
- Gaseous reactant ( $CO_2$ ) diffuses through the product layer to the interface between the product layer and the unreacted sorbent;
- Gaseous reactant ( $CO_2$ ) reacts with the unreacted sorbent particles;
- New product layer generated on the surface of the sorbent particle.

The reaction rate of the  $CO_2$  absorption  $r_{CO_2}$  could be expressed by  $r_{CO_2} = -k_{reaction} \cdot C_{CO_2}$ , where  $k_{reaction}$  is the reaction rate coefficient and  $C_{CO_2}$  is the  $CO_2$  concentration.

The reaction rate constant  $k_{reaction}$  is determined by the Arrhenius equation:

$$k_{reaction} = A e^{-\frac{E_a}{RT}} \quad (14)$$

Where  $A$  is the pre-exponential factor,  $E_a$  is the activation energy for the reaction,  $R$  is the universal gas constant. In this case, the activation energy of the carbonation reaction is about 44.1 kJ/mol and the pre-exponential factor is about 0.0643 m/s [12].

The unreacted radius  $r_i$  could be calculated by the following equation

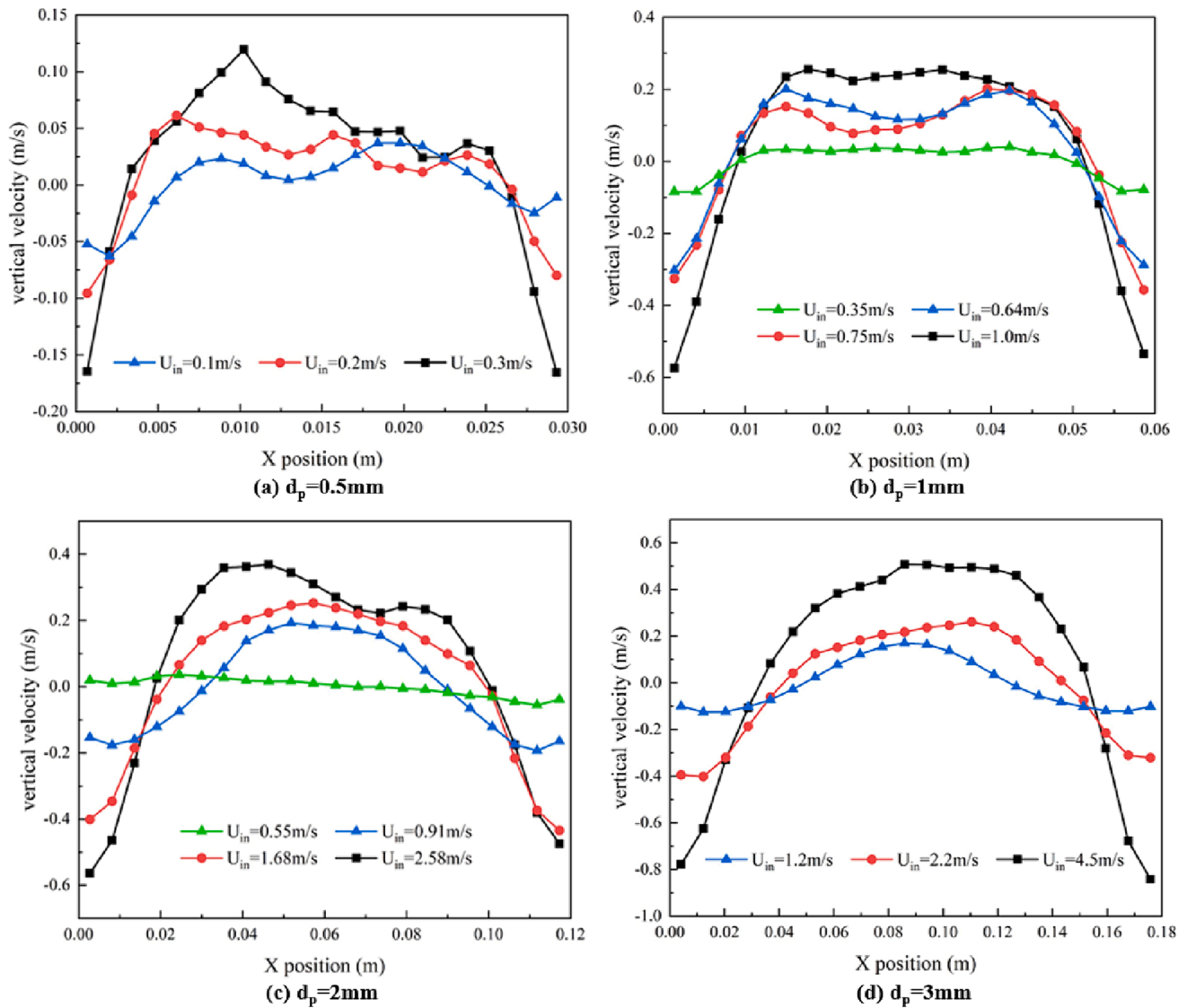


Fig. 9. Time-averaged velocity for different sizes of sorbent particles.

[13]:

$$\frac{dr_i}{dt} = -\frac{k_s}{N_{MgO}^0} \left[ \frac{(C_b - C_e)}{1 + \frac{k_s}{D_g} r_i (1 - \frac{r_i}{r_p})} \right] \quad (15)$$

where  $k_s$  is the constant reaction rate of the surface reaction at different zones: when the reaction occurs on the surface of the highly reactive zone (outer layer of the particle),  $k_s = k_h$ ; when the reaction occurs on the surface of the inner low reactive zone,  $k_s = k_l$ .  $N_{MgO}^0$  is the number of moles of MgO (per unit volume) at the initial state,  $r_p$  is the expanded radius of the sorbent particle,  $C_b$  and  $C_e$  are the bulk gas  $\text{CO}_2$  concentration and equilibrium  $\text{CO}_2$  concentration, respectively.  $D_g$  is product layer diffusivity of  $\text{CO}_2$ , which could be calculated by the equation:

$$D_g = D_{g0} \cdot e^{-\alpha X^\beta} \quad (16)$$

where  $D_{g0}$  is the diffusion coefficient at the initial state;  $\alpha$  and  $\beta$  are two adjustable parameters in the model. The value of  $D_{g0}$  and  $\alpha$  are in terms of temperature [13].  $\beta$  could be obtained through curve fitting by Matlab.

The conversion rate for the sorbent particle is determined by the equation:

$$X = 1 - \left(\frac{r_i}{r_p}\right)^3 \quad (17)$$

where  $r_p$  is the particle radius at the initial state.

Equation (18) describes how the expanded radius  $r_p'$  of the particle can be calculated:

$$r_p' = r_p \sqrt[3]{(1-X) + ZX} \quad (18)$$

in which Z represents the factor of expansion.

Combining equations (15)-(18), the change rate of the conversion rate can be derived from the equation:

$$\frac{dX}{dt} = \frac{\frac{3}{r_p} \frac{k_s}{N_{MgO}^0} (C_b - C_e) (1-X)^{\frac{2}{3}}}{1 + \frac{k_s}{D_g} r_p (1-X)^{\frac{1}{3}} (1 - \sqrt[3]{\frac{1-X}{1-X+ZX}})} \quad (19)$$

### 3. Numerical settings

In this study, two-way coupled CFD-DEM simulations were performed based on the open-source software CFDEM@Coupling [30]. On

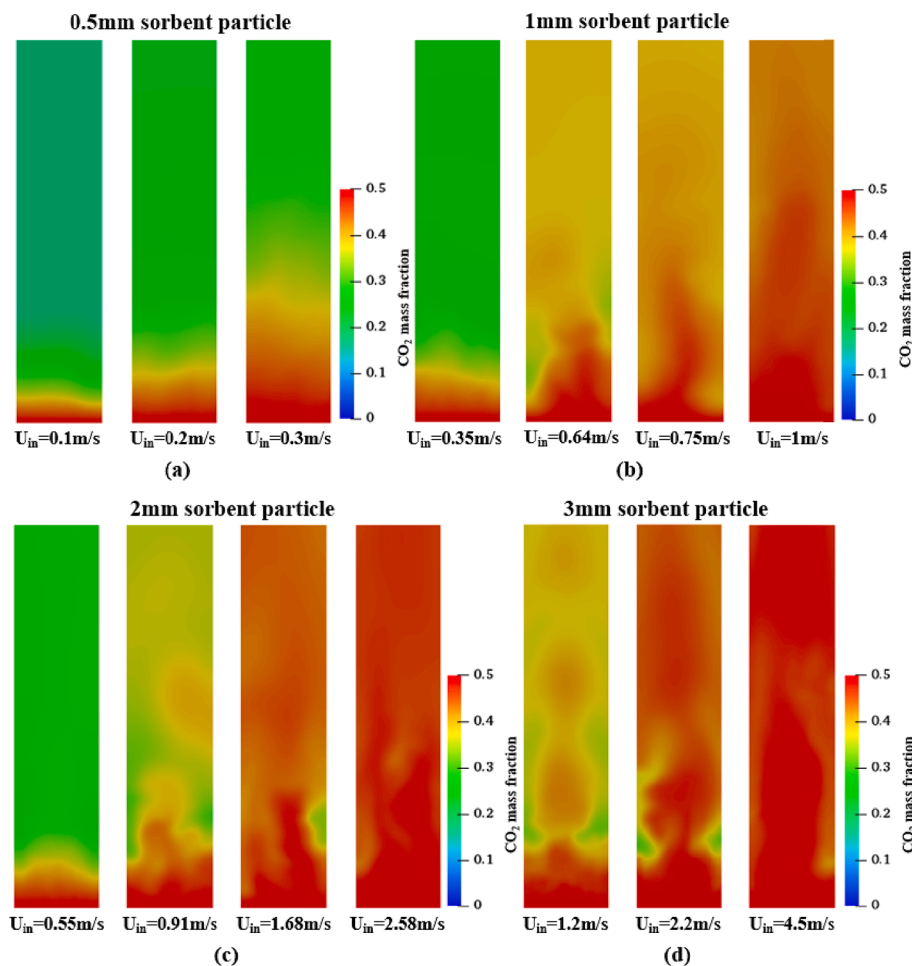


Fig. 10. Instantaneous screenshots at various inlet gas velocities and sorbent particle sizes.

the CFD side, the governing equations were solved by the open-source software OpenFOAM; on the DEM side, the particle motion was simulated by the open-source software LIGGGHTS. Due to the limitations of the computational resources, only a section of the fluidized bed flow field was selected as the subject of the simulation to investigate the local behavior of the flow field and particle motion, as well as the decarbonization performance. Table 1 lists the specific simulation parameters:

## 4. Results and discussion

### 4.1. Validation and mesh dependence

To determine the values of the coefficients and verify the accuracy of the decarbonization model, the shrinking-core model was calculated via Matlab codes as well as the self-developed CO<sub>2</sub> removal solver based on the CFD-DEM model. The parameters applied in the simulations (e.g., adjustable parameters in eq. (13) were determined through curve fitting via Matlab. The simulated results of Matlab ensure the accuracy of parameter values applied in this study, while the simulation case of CFD-DEM model was conducted to verify the particle shrinking model implemented in this study. In Fig. 3, the conversion rate of MgO sorbent is compared between TGA experiment results [34] and simulated results calculated by Matlab codes and the CO<sub>2</sub> removal solver. It could be found that the conversion rate initially increases almost linearly with reaction time, indicating a high reaction rate, but after 120 s, the reaction rate significantly decreases. The simulation results closely align with the experimental findings within acceptable margin of error. This

discrepancy may be due to simplified assumptions about the decarbonization reaction process [28]. In this study, it is assumed that as long as both gaseous reactant and particles are situated within the same computational grid, the reaction would take place; however, the actual reaction dynamics are far more intricate than assumed.

To ensure the accuracy of the selected grid size in this study, we have conducted a verification of grid independence in this section. Fig. 4 illustrates the averaged gas volume fraction corresponding to different bed heights under varying grid sizes. All simulations employ identical boundary conditions, while the grid size ranges from 2.5dp to 3.3dp.

Conclusion could be drawn that for the two coarse grids of 3dp and 3.3dp, there exists a significant deviation in simulation results compared to other cases: when employing a grid size of 3.3dp, the average gas volume fraction within the bed height range of 0.2 ~ 0.4 m is notably smaller than that observed in other cases; conversely, when employing a grid size of 3dp, the average gas volume fraction within the bed height range of 0.1 ~ 0.3 m is quite larger than that observed in other cases. The difference in the cases that apply grid sizes of 2.7dp and 2.5dp is relatively small. After careful evaluation of both computational precision and cost, 2.7dp of grid size has been chosen.

When the inlet gas velocity is larger than the minimum fluidization velocity, the fluidized bed exhibits typical fluidization characteristics. A series of simulations were conducted to figure out the effects of different sizes of solid sorbent particles and different inlet gas velocities on the flow field behavior, particle motion and CO<sub>2</sub> removal performance of the fluidized beds.

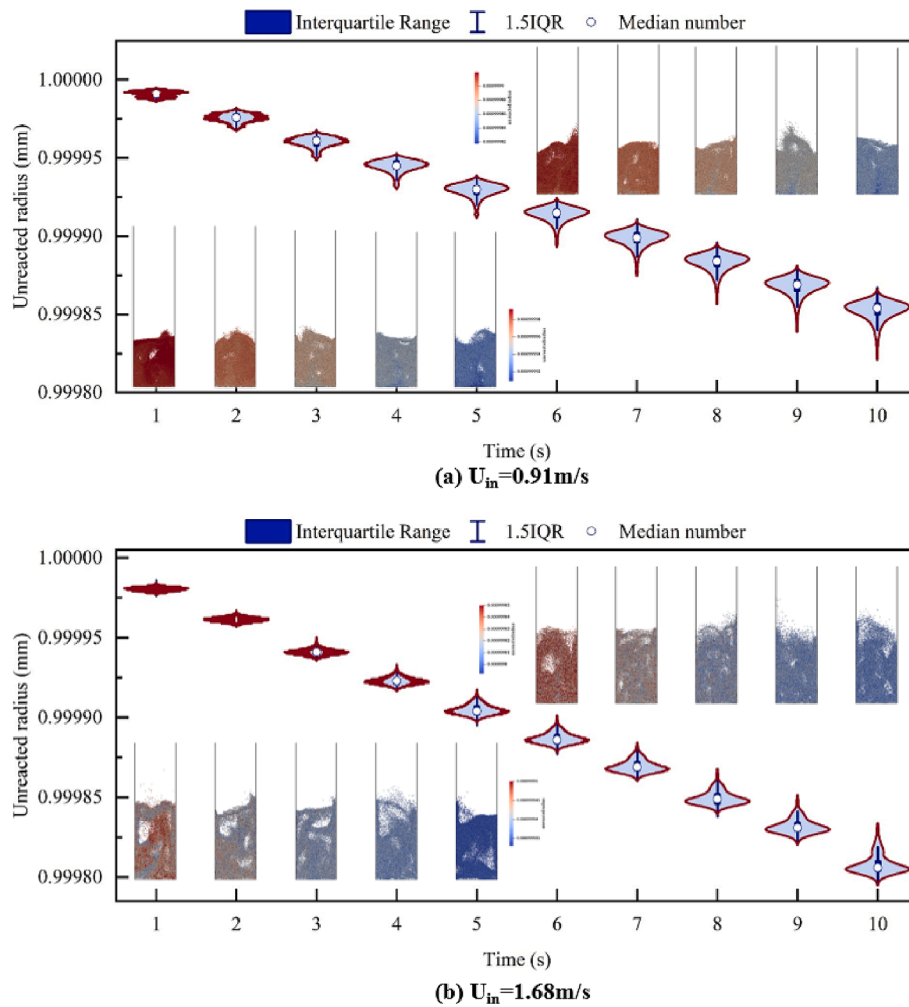


Fig. 11. Violin plot for the unreacted radius of solid sorbent particle with the instantaneous screenshot of particles.

#### 4.2. Flow field behavior

Fig. 5 (a) to (d) plot the instantaneous screenshots of the fluidized bed for different sizes of solid sorbent particles (from 500  $\mu\text{m}$  diameter to 3 mm diameter) and different inlet gas velocities. It could be found that when the inlet gas velocity is relatively small ( $U_{in} < U_{mf}$ ), the fluidized bed exhibits semi-fluidized characteristics, where the particles are partially fluidized and only small bubbles are formed in the system. As the inlet gas velocity increases, the fluidization state becomes much more violent from partly fluidized to fully fluidized and the bed expansion greatly increases. For the smaller sorbent particles (0.5 mm and 1 mm particles), the void fraction in the computational domain predominantly exceeds 0.6, which means that particles are more likely to be fully fluidized and considerable bed expansion could be exhibited. When the bed is fully fluidized, the particles are distributed relatively uniformly throughout the entire reaction duration; for larger sorbent particles (2 mm and 3 mm particles), the void fraction in the computational domain varies between 0.4 ~ 0.6, with slugging modes as well as gas channels observed in the bed. Large bubbles are formed from the bottom of the fluidized bed, resulting in a considerable reduced average bed height compared to that of the smaller solid sorbent particles. It could be summarized that different sizes of solid sorbent particles exhibit varying fluidization characteristics.

To obtain more quantitative data on these cases with different parameters, Fig. 6 depicted the time-averaged void fraction for different sizes of solid sorbent particles and varying inlet gas velocities. It could be noticed that the bed expansion experiences a noticeable increase with

the increase of the inlet gas velocity. For small solid sorbent particles, the averaged void fraction is less than 0.8, whereas the value of larger solid sorbent particles is about 0.85, implying that the bed expansion of larger solid sorbent particles is much higher than that of smaller solid sorbent particles. The particle distribution exhibits enhanced uniformity throughout the reaction period. When the bed is partly fluidized, increasing the diameter of sorbent particles significantly decreases the averaged void fraction in the fluidized bed; when the bed is fully fluidized, solid sorbent particles with different sizes cast only slight influence on the time-averaged void fraction of the fluidized bed. The results indicate that for semi-fluidized bed, increasing the size of solid sorbent particles significantly reduce the bed expansion and the solid sorbent particle are packed much more tightly.

It could be found that for the fully fluidized bed, the difference in particle distribution is not obvious while the bubbles formed in the case of different sorbent particle sizes are different. As a consequence, the analysis of bubble dynamics is necessary. In order to detect bubbles in the fluidized bed system, self-written Matlab codes were applied to record the position and size of bubbles formed at each time step. Fig. 7 shows the probability of equivalent bubble size for varying sizes of solid sorbent particles, from which it could be observed that for smaller solid sorbent particles, the probability of small bubbles is the highest, which is up to 0.45, and as the particle diameter increases, the probability of small bubbles decreases and the probability of medium-sized bubbles increases significantly. For larger particles (2 mm and 3 mm solid sorbent particles), the probability of medium-sized bubbles was the highest, which is up to 0.35. Large bubbles are primarily observed with relatively

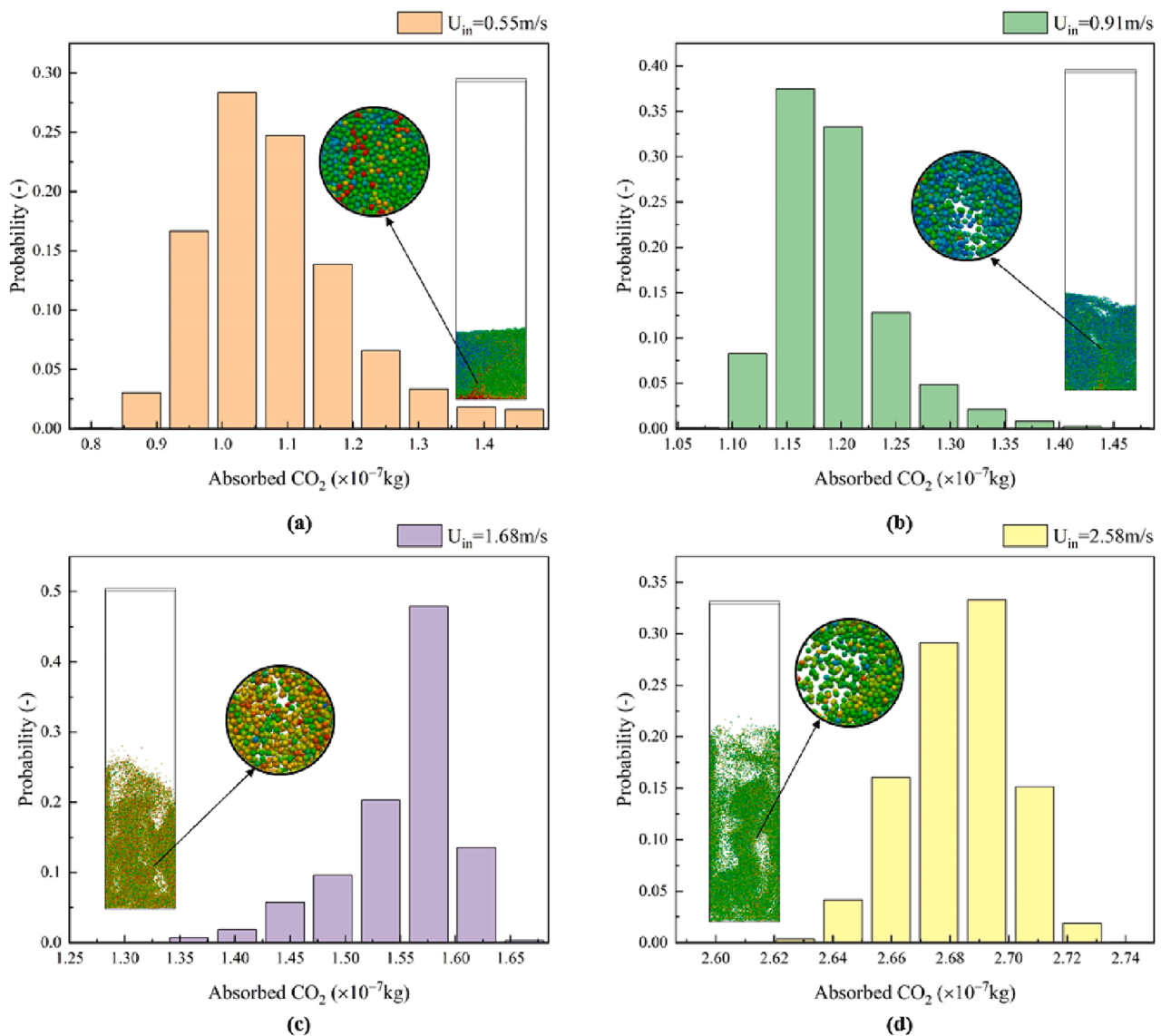


Fig. 12. Probability plot of absorbed CO<sub>2</sub> mass with varying inlet gas velocity.

large sorbent particles. Thus, smaller solid sorbent particles are associated with smaller bubbles, and larger particles with larger bubbles. For smaller solid sorbent particles, only a small number of small bubbles can be detected with higher bed expansion, while for large solid sorbent particles, large bubbles can be found pushing the solids upwards.

#### 4.3. Particle motions

It has been pointed out in the introduction section that pioneering researches mainly regarded the solid phase as Eulerian phase and therefore there is a lack of information on the particle motion. In this study, the moving trajectory of each particle is calculated by Newton's second law and recorded individually. The validation of particle motion can be referenced from our previous work [35]. In this section, the motion of the solid sorbent particles has been analyzed through Fig. 8 and Fig. 9. Fig. 8 plots the time-averaged velocity vectors of the particles, colored by velocity magnitude, clearly highlighting the symmetric motion of particles. The time-averaged velocity vector of particles shows the tendency of particle motion: particles flow upward from the center of the bed and downward from both sides back to the bottom of the bed. As the particle velocity contour shows, small sorbent particles exhibit large bed expansion, while large sorbent particles exhibit greater symmetry.

To quantitatively analyze the motion pattern of solid sorbent particles in the bed, the vertical velocity of the particles is depicted in Fig. 9, based on which it can be stated that the larger the inlet gas velocity, the larger the velocity fluctuations; and the smaller the inlet gas velocity is, the smoother the velocity fluctuation is. For example, for 2 mm solid sorbent particles, when the inlet velocity is 0.55 m/s, the fluctuation amplitude of vertical velocity is about 0.05 m/s; when the inlet velocity increases to 0.91 m/s, the fluctuation amplitude of vertical velocity sharply increases to 0.4 m/s; when the inlet gas velocity continues to increase to 1.68 m/s, the fluctuation amplitude of vertical velocity correspondingly increases to 0.6 m/s; when the inlet velocity increases to 2.58 m/s, the minimum vertical velocity is about -0.6 m/s and the maximum vertical velocity is up to 0.4 m/s, corresponding to a maximum vertical velocity fluctuation of 1 m/s. The symmetry of the particle motion could also be observed in Fig. 9. Similar to the conclusion drawn from Fig. 8, increasing the size of solid sorbent particle could significantly enhance the symmetry of the solid sorbent particle motion in the fluidized bed.

#### 4.4. Gas-solid CO<sub>2</sub> removal performance

The decarbonization performance is one of the most concerned

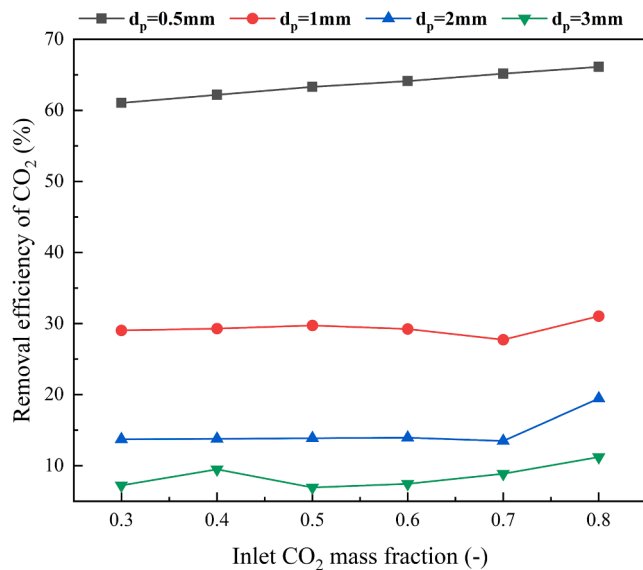


Fig. 13. CO<sub>2</sub> removal efficiency for different sizes of solid sorbent particles with varying inlet CO<sub>2</sub> mass fraction.

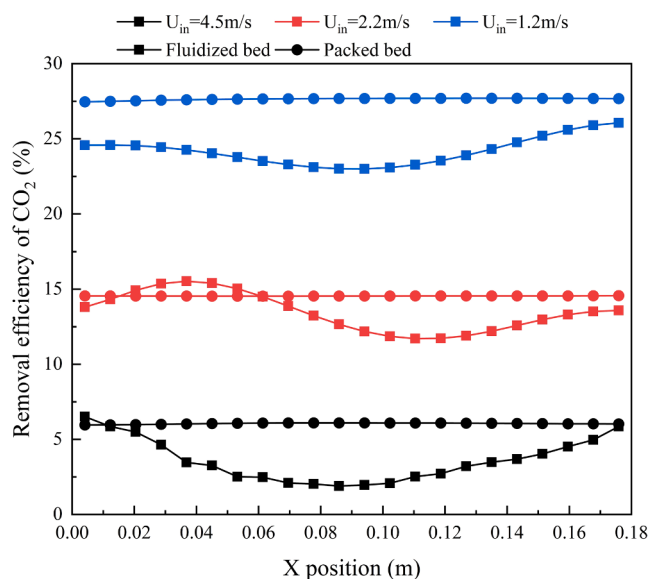


Fig. 14. CO<sub>2</sub> removal efficiency at the outlet of fluidized bed and packed bed (d<sub>p</sub> = 3 mm).

indicators to guide the design of gas–solid fluidized bed for CO<sub>2</sub> removal. In order to figure out the CO<sub>2</sub> removal performance, Fig. 10 displays the instantaneous screenshots colored by CO<sub>2</sub> mass fraction at various inlet gas velocities and sorbent particle sizes. By varying the inlet gas velocity, the effect of gas residence time can be evaluated. As can be seen in Fig. 10, the carbon capture process predominantly occurs at the bottom of fluidized bed where the solid sorbent particles are placed. As the inlet gas velocity increases, there is a decrease in the mass fraction of CO<sub>2</sub> at the outlet, meaning that enhancing the residence time of gas could improve the removal efficiency of CO<sub>2</sub> since longer residence time allows for increased contact time between the sorbent particles and the gas phase. For instance, when the inlet gas velocity increases from 0.35 m/s to 1 m/s, the mass fraction of CO<sub>2</sub> at the outlet increases from 0.3 to 0.4, indicating that the removal efficiency of CO<sub>2</sub> is decreased to 20%. Similar conclusions could be drawn for different sizes of solid sorbent particles. By comparing the mass fraction of CO<sub>2</sub> at the outlet for cases with different sizes of sorbent particles, it can be noticed that decreasing

the diameter of solid sorbent particles also contributes the removal process of CO<sub>2</sub>.

However, it is not possible to achieve excellent decarbonization performance simply by further decreasing the inlet gas velocity or particle size. Decreasing the inlet gas velocity would change the fluidization behavior of the bed from a turbulent fluidization regime to a semi-fluidization regime or even a fixed bed state. In addition, the decrease of the inlet gas velocity also prolongs the total elapsed time of the removal process. For fine particles, the fluidization of the bed is much more turbulent and the existence of cohesive force makes the bed behavior unpredictable: particles are more likely to lose mass to downstream equipment and therefore only suitable for circulating fluidized beds.

Fig. 11 shows the violin plot of the radius of unreacted zone of the solid sorbent particles with the instantaneous screenshots of particles. To save computational resources, only the reaction time period from 1 ~ 10 s is excerpted (the gas–solid reaction occurs mainly on the surface of the outer high-reactive zone). As can be seen, as the reaction occurs, the unreacted radius continues to decrease and shows a linear relationship between the unreacted radius and the reaction time within the time period of 1 ~ 10 s. This could be due to the fact that during the time period of 1 ~ 10 s, the reaction mainly occurs on the surface of the high-reactive zone and the reaction rate is almost linearly correlated with the reaction time as indicated in Fig. 3. The instantaneous screenshots as well as the violin plots also display the distribution of solid sorbent particles with varying unreacted radii. It can be obviously observed that at the beginning of the reaction (time = 1 ~ 3 s), the distribution of unreacted radius is much more irregular and does not obey the kernel smooth rule. As the reaction proceeds, the distribution of unreacted radius obeys the kernel smooth rule. When the inlet gas velocity is 0.91 m/s, solid sorbent particles with medium-sized and large-sized unreacted reaction zones dominate; when the inlet gas velocity increases to 1.68 m/s, solid sorbent particles with small-sized and medium-sized unreacted reaction zones dominate. The results indicate that the increase in gas velocity significantly changes the distribution of unreacted radius of solid sorbent particles. As the inlet gas velocity increases, the probability of solid sorbent particles that own small-sized unreacted zones increases a lot.

To identify the effects of inlet gas velocity on the decarbonization performance of solid sorbent particles, Fig. 12 plots the probability plot of absorbed CO<sub>2</sub> mass with varying inlet gas velocity at time = 10 s (the gas–solid reaction occurs mainly on the surface of the outer high-reactive zone). It could be stated that when the bed is semi-fluidized (U<sub>in</sub> = 0.55 m/s and U<sub>in</sub> = 0.91 m/s), most of the solid sorbent particles only absorb a small amount of CO<sub>2</sub>; when increasing the inlet gas velocity to 1.68 m/s and 2.58 m/s to achieve fully fluidization region, solid sorbent particles that absorbed a relatively large amount of CO<sub>2</sub> dominate. To be more detailed, when the inlet gas velocity is 0.55 m/s, the solid sorbent particles are almost fixed, and the probability of solid sorbent particles with an absorption amount between  $0.99 \times 10^{-7}$  kg CO<sub>2</sub> and  $1.5 \times 10^{-7}$  kg CO<sub>2</sub> is the largest, which are mainly placed at the bottom of the bed. Similarly, when the inlet gas velocity is 0.91 m/s, the probability of solid sorbent particles with an absorption amount between  $1.135 \times 10^{-7}$  kg CO<sub>2</sub> and  $1.175 \times 10^{-7}$  kg CO<sub>2</sub> is the largest. The results indicate that when the bed is semi-fluidized, only a few particles exhibit great decarbonization performance and most particles only absorb a small amount of CO<sub>2</sub>. On the contrary, when the bed is fully fluidized, the probability of the solid sorbent particles that absorbed a relatively large amount of CO<sub>2</sub> increases significantly.

To exclude the effect cast by varying CO<sub>2</sub> concentration, the influence of varying inlet CO<sub>2</sub> concentration was also studied. Fig. 13 compared the decarbonization efficiency of adsorbent particles with varying inlet CO<sub>2</sub> mass fractions, from which it could be summarized that different sizes of solid sorbent particles exhibit various decarbonization characteristics.

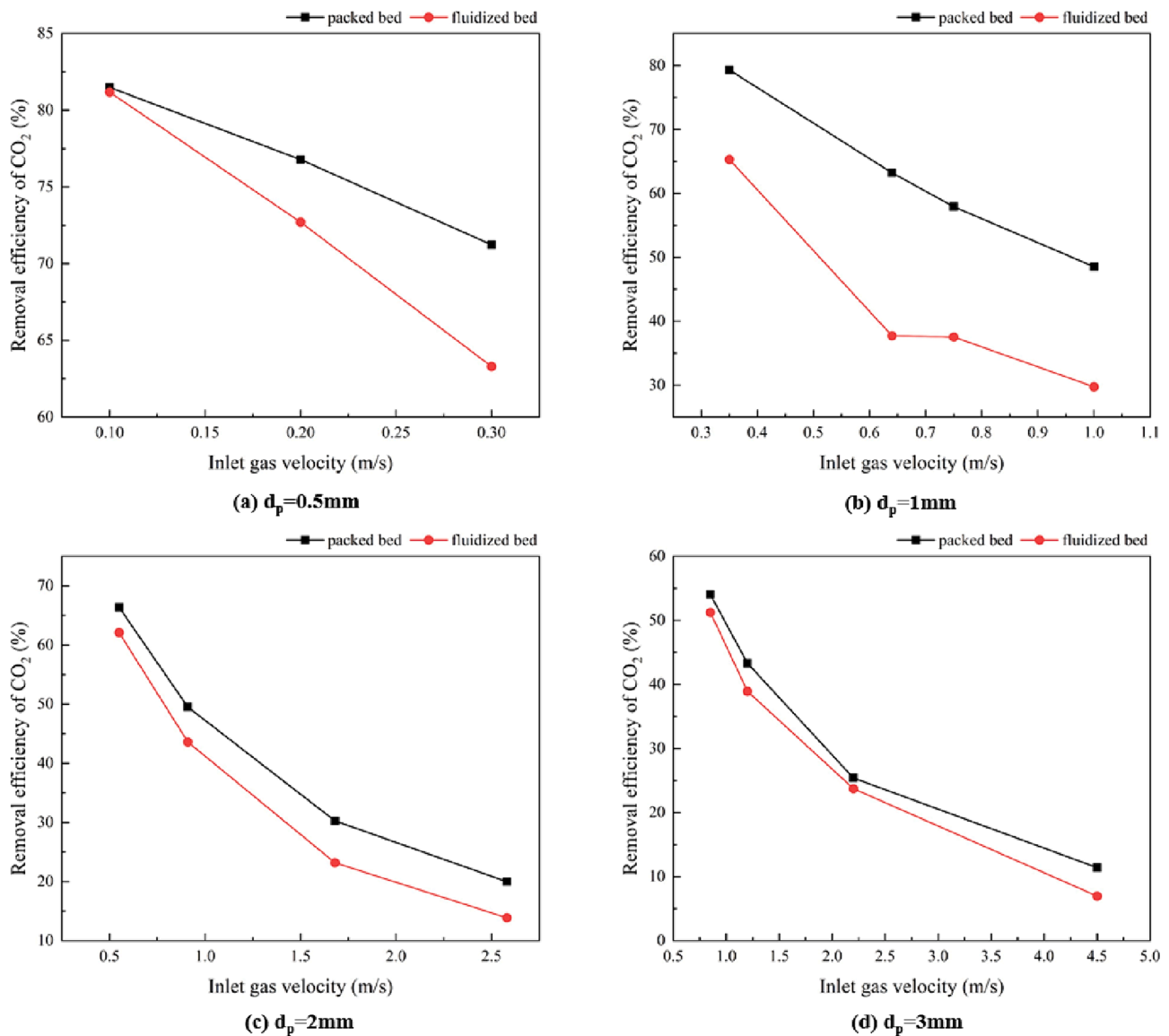


Fig. 15. Average CO<sub>2</sub> removal efficiency for fluidized bed and packed bed with different diameter of solid sorbent particles and inlet gas velocity.

With the increase in inlet CO<sub>2</sub> mass fraction, the CO<sub>2</sub> removal efficiency for smaller solid sorbent particles ( $d_p = 0.5$  mm) increases slightly. Conversely, larger particles show a significantly lower CO<sub>2</sub> removal efficiency. The CO<sub>2</sub> removal efficiency initially increases with a higher inlet CO<sub>2</sub> mass fraction, then decreases, and eventually rises again. This pattern may be attributed to changes in gas density across mesh grids.

#### 4.5. Influence of bed type on decarbonization performance

It is widely recognized that fluidized beds allow continuous input of solid sorbents and provide large inter-phase contact area that is beneficial to heat transfer process. However, the particle conversion rate of the fluidized bed is relatively low. Packed beds offer the advantages of high conversion rate and low erosion of solid sorbent particles in chemical reactions. In this study, similar simulation cases were also carried out on packed beds to figure out the influence of bed type on decarbonization performance, which is helpful to approach the optimal protocol of bed reactors for CO<sub>2</sub> removal.

In previous section, the influence of inlet gas velocity on decarbonization performance was analyzed, and effect of different bed regimes on

decarbonization performance was also observed. In this section, solid sorbent particles were packed at the bottom of the bed with different values of inlet gas velocity and sorbent particle size.

Fig. 14 plots the removal efficiency of CO<sub>2</sub> at the outlet of packed bed and fluidized bed. It can be easily concluded that in the packed bed, the CO<sub>2</sub> removal efficiency is almost constant at the outlet, indicating that the distribution of CO<sub>2</sub> mass fraction at the outlet of the packed bed is much more uniform compared to the fluidized bed. In addition, the packed bed exhibits a slightly higher averaged CO<sub>2</sub> removal efficiency than the fluidized bed, which may be due to the homogeneous distribution of gas flow throughout the packed bed.

To be more quantitative, Fig. 15 displays the average CO<sub>2</sub> removal efficiency for fluidized bed and packed bed with different diameter of solid sorbent particles and inlet gas velocity. As it is observed, for larger solid sorbent particles, the CO<sub>2</sub> removal efficiency of the packed bed is only slightly larger than that of the fluidized bed. The removal efficiency of both fluidized bed and packed bed decrease with the increase of inlet gas velocity. In addition, with increasing inlet gas velocity, the difference in the reduced CO<sub>2</sub> removal efficiency becomes smaller. For small solid sorbent particles, it could be observed that although the decarbonization efficiency decreases with increasing inlet gas velocity for

both fluidized bed and packed beds, the difference in CO<sub>2</sub> removal efficiency between the packed bed and fluidized bed is obvious. For the packed bed, the removal efficiency decreases almost linearly with the increase of inlet gas velocity. As for the fluidized bed, the relationship between the CO<sub>2</sub> removal efficiency and inlet gas velocity is heterogeneous, which may be due to the irregular turbulent gas flow of the fluidized bed. The more irregular the turbulent flow of fluidized bed, the more difficult to predict its decarbonization performance. It could be summarized that packed beds exhibit relatively larger removal efficiency and more uniform gas flow, while fluidized beds provide larger contact area between the gas phase and solid sorbent particles.

## 5. Conclusions

In this study, the removal of CO<sub>2</sub> by solid particles based on MgO adsorbent was modelled in a gas–solid fluidized bed, and the fluid hydrodynamics, particle motions, and CO<sub>2</sub> removal performance were investigated by CFD-DEM two-way coupled numerical simulations. With the analysis of varying particle radius (different type of Geldart particles), inlet gas velocity (different type of fluidized bed reactors) and inlet CO<sub>2</sub> concentration, the results are helpful to explore the optimal protocol of bed reactors for CO<sub>2</sub> removal. Main conclusions are shown as the following:

1. The moving trajectory of each particle was individually tracked, allowing for quantitative calculation of CO<sub>2</sub> absorption capacity based on the shrinking-core model
2. The effects of solid sorbent particle size, inlet gas velocity, and inlet CO<sub>2</sub> mass fraction were simulated. It was found that utilizing lower inlet gas velocities (providing longer residence time and significantly improving CO<sub>2</sub> removal efficiency by over 50 %), smaller solid adsorbent particles (providing larger contact area between phases and exceeding 60 % improvement), and higher CO<sub>2</sub> mass fractions (especially for smaller sorbent particles) can effectively enhance the removal efficiency of CO<sub>2</sub>.
3. The decarbonization performance of fluidized bed and packed bed was compared. The packed bed exhibits a higher decarbonization efficiency and a more uniform gas flow, while the fluidized bed provides a larger contact area between the gas phase and the solid particles, which is beneficial for the heat transfer process.

## CRedit authorship contribution statement

**Linhang Zhu:** Writing – original draft, Validation, Software. **Chang Liu:** Formal analysis, Data curation. **Chenghang Zheng:** Writing – review & editing, Supervision, Funding acquisition. **Shihan Zhang:** Writing – review & editing. **Haidong Fan:** Resources. **Kun Luo:** Supervision. **Xiang Gao:** Conceptualization, Supervision.

## Declaration of competing interest

The authors declare that they have no known competing financial interests or personal relationships that could have appeared to influence the work reported in this paper.

## Data availability

Data will be made available on request.

## Acknowledgement

This research presented in this paper received support from the National Key Research and Development Program of China (No.2022YFC3701500), the Fundamental Research Funds for the Central Universities (No.2022ZJFH004), the National Natural Science Foundation of China (Nos.52076191 and 42341208).

## References

- [1] S.-Y. Pan, P.-C. Chiang, W. Pan, H. Kim, Advances in state-of-art valorization technologies for captured CO<sub>2</sub> toward sustainable carbon cycle, *Crit. Rev. Environ. Sci. Technol.* 48 (5) (2018) 471–534.
- [2] Aresta M. Carbon Dioxide: Utilization Options to Reduce its Accumulation in the Atmosphere. In: *Carbon Dioxide as Chemical Feedstock*; 2010. pp. 1–13.
- [3] Z. Zhang, D.-N. Vo, T.B.H. Nguyen, J. Sun, C.-H. Lee, Advanced process integration and machine learning-based optimization to enhance techno-economic-environmental performance of CO<sub>2</sub> capture and conversion to methanol, *Energy* 293 (2024) 130758.
- [4] Z. Zhang, S.-Y. Pan, H. Li, J. Cai, A.G. Olabi, E.J. Anthony, et al., Recent advances in carbon dioxide utilization, *Renew. Sustain. Energy Rev.* 125 (2020) 109799.
- [5] T. He, Z. Liu, H. Son, T. Gundersen, W. Lin, Comparative analysis of cryogenic distillation and chemical absorption for carbon capture in integrated natural gas liquefaction processes, *J. Clean. Prod.* 383 (2023) 135264.
- [6] Z. Dai, L. Deng, Membranes for CO<sub>2</sub> capture and separation: Progress in research and development for industrial applications, *Sep. Purif. Technol.* 335 (2024) 126022.
- [7] J. Xiang, D. Wei, W. Mao, T. Liu, Q. Luo, Y. Huang, et al., Comprehensive kinetic study of carbon dioxide absorption in blended tertiary/secondary amine solutions: Experiments and simulations, *Sep. Purif. Technol.* 330 (2024) 125310.
- [8] H. Ren, H. Zhang, W. Li, Z. Tang, D. Zhang, Simulation of CO<sub>2</sub> capture process in gas-solid bubbling fluidized bed by computational mass transfer, *J. Environ. Chem. Eng.* 10 (5) (2022).
- [9] D.Y.C. Leung, G. Caramanna, M.M. Maroto-Valer, An overview of current status of carbon dioxide capture and storage technologies, *Renew. Sustain. Energy Rev.* 39 (2014) 426–443.
- [10] Y. Ju, C.-H. Lee, Dynamic modeling of a dual fluidized-bed system with the circulation of dry sorbent for CO<sub>2</sub> capture, *Appl. Energy* 241 (2019) 640–651.
- [11] Y. Zhou, Y. Han, Y. Lu, H. Bai, X. Hu, X. Zhang, et al., Numerical simulations and comparative analysis of two- and three-dimensional circulating fluidized bed reactors for CO<sub>2</sub> capture, *Chin. J. Chem. Eng.* 28 (12) (2020) 2955–2967.
- [12] A. Hassanzadeh, J. Abbasian, Regenerable MgO-based sorbents for high-temperature CO<sub>2</sub> removal from syngas: 1. Sorbent development, evaluation, and reaction modeling, *Fuel* 89 (6) (2010) 1287–1297.
- [13] E. Abbasi, A. Hassanzadeh, J. Abbasian, Regenerable MgO-based sorbent for high temperature CO<sub>2</sub> removal from syngas: 2. Two-zone variable diffusivity shrinking core model with expanding product layer, *Fuel* 105 (2013) 128–134.
- [14] E. Abbasi, A. Hassanzadeh, S. Zarghami, H. Arastoopour, J. Abbasian, Regenerable MgO-based sorbent for high temperature CO<sub>2</sub> removal from syngas: 3. CO<sub>2</sub> capture and sorbent enhanced water gas shift reaction, *Fuel* 137 (2014) 260–268.
- [15] E. Abbasi, J. Abbasian, H. Arastoopour, CFD-PBE numerical simulation of CO<sub>2</sub> capture using MgO-based sorbent, *Powder Technol.* 286 (2015) 616–628.
- [16] E. Ghadirian, J. Abbasian, H. Arastoopour, Three-dimensional CFD simulation of an MgO-based sorbent regeneration reactor in a carbon capture process, *Powder Technol.* 318 (2017) 314–320.
- [17] E. Ghadirian, J. Abbasian, H. Arastoopour, CFD simulation of gas and particle flow and a carbon capture process using a circulating fluidized bed (CFB) reacting loop, *Powder Technol.* 344 (2019) 27–35.
- [18] Y. Shen, J. Ma, D. Liu, Y. Wu, J. Zhong, X. Chen, et al., Two-dimensional full-loop simulation of CO<sub>2</sub> capture process in a novel dual fluidized bed system, *Fuel Process. Technol.* 205 (2020).
- [19] T. Shimizu, T. Hirama, H. Hosoda, K. Kitano, M. Inagaki, K. Tejima, A twin fluid-bed reactor for removal of CO<sub>2</sub> from combustion processes, *Chem. Eng. Res. Des.* 77 (1) (1999) 62–68.
- [20] A. Charitos, C. Hawthorne, A.R. Bidwe, S. Sivalingam, A. Schuster, H. Spliethoff, et al., Parametric investigation of the calcium looping process for CO<sub>2</sub> capture in a 10kWh dual fluidized bed, *Int. J. Greenhouse Gas Control* 4 (5) (2010) 776–784.
- [21] B. Chalermisinsuwan, P. Piumsomboon, D. Gidaspow, A computational fluid dynamics design of a carbon dioxide sorption circulating fluidized bed, *AIChE J.* 56 (11) (2010) 2805–2824.
- [22] M. Ayobi, S. Shahhosseini, Y. Behjat, Computational and experimental investigation of CO<sub>2</sub> capture in gas–solid bubbling fluidized bed, *J. Taiwan Inst. Chem. Eng.* 45 (2) (2014) 421–430.
- [23] M.S. van Buijtenen, N.G. Deen, S. Heinrich, S. Antonyuk, J.A.M. Kuipers, A discrete element study of wet particle–particle interaction during granulation in a spout fluidized bed, *Can. J. Chem. Eng.* 87 (2) (2009) 308–317.
- [24] R.W. Breault, E.D. Huckaby, Parametric behavior of a CO<sub>2</sub> capture process: CFD simulation of solid-sorbent CO<sub>2</sub> absorption in a riser reactor, *Appl. Energy* 112 (2013) 224–234.
- [25] S. Clark, D.M. Snider, J. Spenik, CO<sub>2</sub> adsorption loop experiment with Eulerian-Lagrangian simulation, *Powder Technol.* 242 (2013) 100–107.
- [26] E.M. Ryan, D. DeCroix, R. Breault, W. Xu, E.D. Huckaby, K. Saha, et al., Multi-phase CFD modeling of solid sorbent carbon capture system, *Powder Technol.* 242 (2013) 117–134.
- [27] P. Chaiwang, D. Gidaspow, B. Chalermisinsuwan, P. Piumsomboon, CFD design of a sorber for CO<sub>2</sub> capture with 75 and 375 micron particles, *Chem. Eng. Sci.* 105 (2014) 32–45.
- [28] X. Wang, S. Wang, R. Wang, Z. Yuan, B. Shao, J. Fan, Numerical simulation of semi-dry desulfurization spouted bed using the discrete element method (DEM), *Powder Technol.* 378 (2021) 191–201.
- [29] X. Wang, Y. Li, T. Zhu, P. Jing, J. Wang, Simulation of the heterogeneous semi-dry flue gas desulfurization in a pilot CFB riser using the two-fluid model, *Chem. Eng. J.* 264 (2015) 479–486.

- [30] C. Goniva, C. Kloss, N.G. Deen, J.A.M. Kuipers, S. Pirker, Influence of rolling friction on single spout fluidized bed simulation, *Particuology* 10 (5) (2012) 582–591.
- [31] Y. Zhou, H. Li, M. Zhu, X. Hu, H. Yuan, S. Jiang, et al., Effects of liquid content and surface tension on fluidization characteristics in a liquid-containing gas–solid fluidized bed: A CFD–DEM study, *Chem. Eng. Process. - Process Intensif.* 153 (2020) 107928.
- [32] H.P. Zhu, Z.Y. Zhou, R.Y. Yang, A.B. Yu, Discrete particle simulation of particulate systems: Theoretical developments, *Chem. Eng. Sci.* 62 (13) (2007) 3378–3396.
- [33] L. Zhu, Y. Tang, Effects of acoustic fields on the dynamics of micron-sized particles in a fluidized bed, *Powder Technol.* 372 (2020) 625–637.
- [34] G. Xu, Q. Guo, T. Kaneko, K. Kato, A new semi-dry desulfurization process using a powder-particle spouted bed, *Adv. Environ. Res.* 4 (1) (2000) 9–18.
- [35] L. Zhu, Z. Zhao, C. Liu, W. Li, Y. Zhang, Y. Zhang, et al., CFD-DEM simulations of a fluidized bed with droplet injection: Effects on flow patterns and particle behavior, *Adv. Powder Technol.* 34 (1) (2023) 103897.